Magnetic-circular-dichroism study of the valence states of perpendicularly magnetized Ni(001) films

W. Kuch, A. Dittschar, K. Meinel, M. Zharnikov, C. M. Schneider, and J. Kirschner
Max-Planck-Institut für Mikrostrukturphysik, Am Weinberg 2, D-06120 Halle, Germany

J. Henk and R. Feder
Theoretische Festkörperphysik, Universität Duisburg, D-47048 Duisburg, Germany
(Received 20 October 1995)

Magnetic circular dichroism in valence-band photoemission from perpendicularly magnetized Ni thin films on Cu(001) has been studied both experimentally and theoretically. Over the photon energy range of 11–27 eV for normal emission and normal incidence, intensity asymmetries up to 20% upon light helicity or magnetization direction reversal were found. Fully relativistically calculated photoemission spectra agree well with experiment and reveal the interplay between spin-orbit coupling and exchange splitting, which is at the origin of magnetic dichroism. From comparison of theory and experiment the band dispersion is determined and points of hybridization along the Δ axis are identified.

I. INTRODUCTION

As is well known, the electronic structure of metals is influenced significantly by spin-orbit coupling.[1–4] A variety of effects including spin polarization of photoelectrons in paramagnets[5–7] and the polar Kerr effect, owe their existence to the presence of spin-orbit coupling. Great effort has been put, especially in the last few years, in the investigation of spin-orbit-induced effects[8–10] and it has turned out that even in the valence-band structure of low Z materials, as for example Cu, spin-orbit coupling is significant.[11,12]

Magnetic dichroism in photoemission or absorption, which is the modification of intensity-distribution curves by reversal of the magnetization direction, is exclusively due to the interplay of spin-orbit and exchange coupling (see for example Refs. 13–16). Magnetic dichroism in x-ray absorption as well as in core-level photoemission probes the interaction of spin-orbit split core levels with spin polarized valence electrons. It is hence considered as a tool for element-specific investigations of magnetic properties. For the determination of the electronic band structure, angle-resolved photoemission spectroscopy (ARPES) of valence electrons is one of the most commonly used and powerful methods.[8,17,18] Magnetic circular dichroism in the angular distribution (MCDAD) of valence-band photoemission is caused by the interplay between exchange-splitting and spin-orbit coupling in the valence states. ARPES with the extension of measuring the accompanying MCDAD therefore is a most appropriate tool for the direct investigation of the electronic structure of ferromagnets, including both exchange and spin-orbit coupling.

For MCDAD from core levels, calculations for single atoms reproduce qualitatively the experimentally observed findings (see, for example, Refs. 14, 19, and 20). Recent experiments, however, show effects on the MCDAD asymmetry due to the crystallinity of the sample; in other words, they reveal the limits of atomic calculations.[21,22]

The interpretation of magnetic dichroism in valence-band photoemission is more complicated than that in core-level photoemission. The knowledge of both the detailed valence- and conduction-band structures of the semi-infinite crystal is necessary to interpret adequately the experimental findings. Using an experimental arrangement of high symmetry facilitates the interpretation by means of dipole selection rules. For normally incident circularly polarized light and normal emission of photoelectrons from an (001) surface of a cubic crystal, selection rules allow only transitions from valence states with Δ^5 single-group symmetry spatial parts into final states with Δ^1 symmetry.[23] Furthermore, the photoelectron spin polarization is complete[23,24] and is aligned with the direction of light incidence.[11,12,25–27] The presence of a magnetization generally reduces the symmetry of the semi-infinite solid, however, when it is perpendicular to the crystal surface, the surface normal remains a rotation axis, and the electronic states can still be classified according to irreducible double-group representations of the nonmagnetic case.[15,28] Such a totally symmetric geometry thus opens the possibility to discuss the MCDAD in terms of a simple interband transition model, including both spin-orbit coupling and exchange interaction.

The purpose of the present paper is to relate the valence-band magnetic circular dichroism in Ni to the underlying band structure. Starting with a simple picture of band symmetries and selection rules, a thorough comparison with fully relativistic band-structure calculations provides a deeper insight into the details of the band structure. Points of hybridization between bands of different spin occupancy and different orbital symmetry, where the expectation value of the spin polarization is low and the illustrative picture ceases to work, may be identified this way. Whereas the main MCDAD features can be qualitatively explained by the symmetry of the involved initial states, extended statements on the origin of all of the observed dichroic features and their relation to exchange and spin-orbit coupling are only possible with access to fully relativistic photoemission calculations. The procedure is to check as a first step the input

parameters for the calculations by comparison of the experimental spectra to one-step photoemission calculations. The next step is to correlate specific dichroic features to the calculated relativistic band structure. This serves to finally end up with an experimental determination of the exchange- and spin-orbit split band structure, which may in details of dispersion and hybridization quite possibly differ from the calculated one.

The chosen system to do this is that of an epitaxial Ni film deposited on a Cu(001) substrate. The interplay between exchange and spin-orbit interaction can be preferably observed in nickel as a prototype system, where both interactions are of the same order of magnitude ($\approx 0.3/0.1$ eV). The relatively small exchange splitting in nickel compared to that of iron or cobalt has the advantage that there are extended regions in the Brillouin zone in which both corresponding majority and minority bands are occupied. The dispersion of such bands may thus be followed experimentally over a distinct range of **k** by photoemission spectroscopy. The observed dichroism also exhibits more spectral features when both majority and minority states contribute to the photoemission signal, which is advantageous for the unambiguous correlation to certain electronic states of the band structure.

Furthermore, for Ni(001) as a prototype case one-step photoemission calculations have already been performed to demonstrate the origin of specific features in MCDAD spectra.[15] Calculated photoemission spectra for normal electron emission from perpendicularly magnetized Ni(001) were presented for both helicities of the incoming circularly polarized UV radiation. The calculated spectral features of the magnetic circular dichroism could be correlated to relativistic band-structure calculations and were discussed by means of direct transitions.

The choice of the Ni/Cu thin-film system was also governed by other considerations. For the reasons mentioned above it is advantageous to have a magnetization perpendicular to the sample surface. For bulk Ni the easy axis of the magnetization is the [111] direction, thus prohibiting the totally symmetric configuration with the vectors of photon and electron momentum, light helicity, and magnetization all collinear with the [001] surface normal. In ultrathin magnetic films, however, other contributions to the magnetic anisotropy due to the shape and the influence of surface and interface of the thin-film system as well as magneto-elastic contributions to the magnetocrystalline anisotropy can lead to different orientations of the magnetization direction. In most of the cases the predominant influence of the magnetic dipole interaction, the shape anisotropy, results in an easy direction parallel to the film plane. In a number of special cases and for limited thickness ranges, there is the possibility that the shape anisotropy can be overcome by other contributions to the magnetic anisotropy related directly to the thin-film nature of the system.[29–31] In such a case the total anisotropy may manifest itself in a resulting magnetization direction perpendicular to the film surface. It is therefore important to select an appropriate substrate to induce the required anisotropic properties in the epitaxially deposited ferromagnetic film. It is reported in the literature that thin films of Ni deposited on a Cu(001) substrate exhibit a perpendicular orientation of the easy axis of magnetization over an extended thickness range.[32–34] The published values of the film thicknesses for perpendicular magnetization vary between 7 and 10 ML for the lower limit and between 56 and 75 ML for the upper limit.[33,34] This is at present the highest film thickness where a simple magnetic overlayer shows a perpendicular magnetization. It is attributed to the magneto-elastic volume anisotropy caused by substrate-induced strain in the epitaxial Ni film.[34–36] The Ni/Cu(001) system thus offers the unique possibility to study the magnetic circular dichroism for a perpendicular magnetization at relatively high film thicknesses, where the electronic structure can be thought of as bulklike. Because of the strain in the film the electronic structure will of course not be fully identical to that of bulk Ni. However, there are no indications for a nonhomogeneous crystalline structure over the whole film thickness,[34,37] so that the magnetic circular dichroism can be studied in the advantageous fully symmetric configuration as provoked by the bulklike electronic structure of the homogeneously strained Ni film.

The origin of the perpendicular anisotropy of Ni/Cu(100) itself is also of great interest. Perpendicularly magnetized films of some ten monolayers are much more favorable for technological applications than those of just one monolayer. The contributions to the magnetic anisotropy overcompensating the in-plane magnetic dipole energy are directly related to the spin-orbit coupled electronic structure of the system. To explore the relativistic band-structure may therefore help to identify the nature of this anisotropy together with supplementary work on structure and morphology of the films.

The organization of this paper is as follows: In the next section details of the experiment are described. In Sec. III the computational method is presented, and the origin of MCDAD in the present geometry is discussed analytically. Both experimental and theoretical results are presented in Sec. IV. In Sec. V they are correlated to the relativistic band structure, and specific information about the electronic structure of the system is drawn from the comparison of experiment and theory.

II. EXPERIMENTAL ASPECTS

The experiments were carried out in a UHV chamber (base pressure 1×10^{-8} Pa) equipped with facilities for low-energy electron diffraction (LEED), Auger electron spectroscopy (AES), magneto-optical Kerr effect (MOKE), medium energy electron diffraction (MEED), and thin-film growth. Details of the setup can be found in Ref. 38.

Nickel was evaporated from a high-purity nickel rod by electron bombardment. Typical deposition rates were 0.5 ML/min, while the overall pressure in the chamber did not exceed 2×10^{-8} Pa. No surface contamination above the AES detection limit ($\approx 1\%$) could be detected after nickel deposition. The sample temperature during deposition was 300 K. All experiments presented in this publication refer to film thicknesses of 15 ML. This is well in the range of perpendicular magnetization, the presence of which was checked before and after acquisition of photoelectron spectra by means of polar MOKE measurements. All films produced rectangular hysteresis loops at room temperature. During the collection of the photoemission spectra presented here the sample temperature was maintained at 300 K.

MEED measurements during Ni evaporation exhibit dis-

tinct oscillations in the specular beam intensity for the first five monolayers, indicating layer-by-layer growth. This is followed by a three-dimensional film growth at higher thicknesses manifesting itself in a monotonously decreasing MEED specular beam intensity. This growth behavior was also observed by scanning tunneling microscopy measurements.[37] The films showed a (1×1) LEED pattern identical to that of the clean Cu substrate, from which a pseudomorphic fcc structure with the lateral lattice constant of Cu(100) is concluded. In order to determine a tetragonal distortion often observed in pseudomorphic fcc films with a certain lattice mismatch to the substrate, LEED-$I(V)$ measurements of the (00) beam were performed. From the shift of energetic positions of the sequence of single-scattering Bragg maxima $6.0\%\pm0.3\%$ compression of the vertical layer spacing with respect to the copper substrate is obtained. This is slightly less that one would expect assuming constant atomic volumes of the nickel atoms, which leads to a value of 6.9%.

To minimize the film roughness, the sample is heated to 450 K for 10 min immediately after completion of the deposition. This procedure is reported to result in flat pseudomorphic films of good quality without copper segregation.[37,39] After the annealing procedure, no change of structure or magnetization could be detected, and the AES Ni to Cu intensity ratio remained identical.

Photoemission spectra were taken at the 6.5 m normal-incidence monochromator beamline of the Berlin synchrotron radiation facility (BESSY), with circular polarization of about 90%.[40] As already discussed in Sec. I, the spectra presented in this paper were taken in the totally symmetric configuration, i.e., normal incidence of the incoming radiation and normal emission of the outgoing photoelectrons.

The electron spectrometer is described in detail elsewhere.[11] It was operated at a fixed pass energy of 8 eV, resulting in an overall energy resolution of approximately 200 meV (including the monochromator resolution). The angular acceptance can be estimated to be less than $\pm2°$. To rule out apparatus-induced asymmetries, spectra for both helicities of the incoming light were taken for both magnetization directions of the sample. The magnetization was reversed after approximately 1 h measuring time, whereas the light helicity was changed after each scan of about 5 min.

All spectra in this paper are shown normalized to the photon flux. This is done by considering the energy dependence of the monochromator photon flux for both gratings from Ref. 40 and normalizing to the ring current. Due to variations of the beam position and size with the ring current, the relation between photon flux at the sample and the ring current is nonlinear. Normalizing linearly with the ring current would result in too small (large) intensities at high (low) ring currents. To account for this effect, the relation between photon flux and ring current was extracted from measurements at constant photon energy for different ring currents and used for the normalization procedure. The remaining uncertainty in comparing experimental intensities at different photon energies is in the range of about 10%.

III. THEORETICAL ASPECTS

A. Computational details

Theoretical photoemission spectra and the corresponding bulk band structure were obtained by fully relativistic calculations of the layer Korringa-Kohn-Rostoker type using a Green's-function formalism.[41] In this method, spin-orbit coupling and exchange interaction are included on an equal footing. Photoelectron spectra are calculated within the one-step model involving relativistic dipole-transition-matrix elements to time-reversed LEED states of the semi-infinite solid. Hole lifetime is incorporated from the start. Our method is strictly valid at $T=0$ K and in good approximation at temperatures well below the Curie temperature.

The effective quasiparticle potential is taken in the muffin-tin shape approximation, which is adequate for closely packed metallic systems. Its spin-dependent real part inside the muffin-tin spheres is adopted from a bulk potential, which we calculated self-consistently by the linear muffin-tin orbital method. Since for Ni this leads to exchange splittings of about 0.6 eV as opposed to an average value of 0.3 eV observed in photoemission experiments, we modified it by an *ad hoc* spin-dependent self-energy correction reducing the splitting between the majority- and the minority-spin potentials by a factor of 0.5. The real part of the inner potential is chosen as 14.67 eV for initial and as $14.67-0.15(E-E_F)$ for the final states. For the imaginary part we adopt energy-dependent forms increasing (in absolute value) away from the Fermi energy E_F as $0.025(E-E_F)$ for the lower and as $0.03(E-E_F)^{1.25}$ for the upper states. The surface potential barrier is simply approximated by a reflecting (nonreflecting) step for the lower (upper) states.

For the geometrical structure of the Ni film we assume a tetragonally-distorted fcc lattice (fct) with the in-plane lattice constant of bulk Cu, namely 2.55 Å (compared to 2.49 Å for bulk Ni). The vertical layer spacing is suggested as 1.69 Å by the results of our LEED-$I(V)$ measurements, which indicate a 6% tetragonally compressed fcc structure (bulk value of Ni: 1.76 Å). All layer spacings of the atomic layers were taken to be equal, thus neglecting possible relaxations in the vicinity of the surface. Because we found experimentally no emission from the Cu substrate, we calculated the photoemission spectra and the bulk band structure for a semi-infinite Ni crystal (with the above fct structure) instead of a 15 layer Ni slab on top of the Cu substrate.

The tetragonal distortion of the Ni lattice, i.e., the decrease of the interlayer spacing compared to the fcc case with Cu lattice constant, increases the dispersion of the bulk bands, as is expected. The band structure for the present fct structure is rather similar to that of bulk-fcc Ni. Differences are obtained in the position of the spin-orbit-induced band gaps. In photoemission, spectra obtained for the three different Ni lattices, namely the tetragonally distorted lattice, the bulk Ni lattice, and the undistorted fcc lattice with the Cu lattice constant, show the same general shape. Minor peaks and shoulders, which are brought about by spin-orbit coupling, differ slightly in intensity and energy position.

B. Analytical considerations

Before turning to the experimental results and their interpretation, it is useful to present briefly some analytical results on MCDAD. The presence of perpendicular magnetization reduces the symmetry of the (001) surface from C_{4v} to C_4, because each mirror operation reverses the magnetiza-

tion and, thus, is no symmetry operation of the entire system. The electronic states can be classified according to four one-dimensional irreducible representations of the double group. Instead of the nomenclature of Falicov and Ruvalds[42] we prefer to use the one of the nonmagnetic system,[15] since the reader is likely to be more familiar with the latter. Because magnetic exchange breaks the time-reversal symmetry, i.e., Kramer's degeneracy is lifted, each of the two-dimensional irreducible double-group representations Δ_6 and Δ_7 of the nonmagnetic case decomposes into a pair of one-dimensional representations, i.e., Δ_6+, Δ_6-, Δ_7+, and Δ_7-. The basis functions of these obey the relations $\hat{T}|\Delta_i+\rangle=|\Delta_i-\rangle$ and $\hat{T}|\Delta_i-\rangle=-|\Delta_i+\rangle$, $\hat{T}$ denoting the time-reversal operator and $i=6,7$. It is important to note that the $+$ $(-)$ sign does not refer to ''majority'' (''minority'') spin because the latter is not a ''good quantum number'' in the presence of spin-orbit coupling. All the above irreducible representations comprise basis functions with spin-up and basis functions with spin-down Pauli spinors. For example, the double-group representation Δ_6+ has basis functions Δ_6^1+, with Δ^1 spatial symmetry and spin-up, and Δ_6^5+, with Δ^5 spatial symmetry and spin-down. The actual states of the semi-infinite crystal are linear combinations of these two types of basis functions.

After calculating the spin-density matrix for photoemission with circularly polarized light, we obtain analytical expressions for the intensity $I(\sigma_\pm)$ and the electron-spin polarization $P_z(\sigma_\pm)$, where $\sigma_\pm$ indicates the helicity of the incident light. P_z can only assume the values $+1$ and -1, and the in-plane polarization components are identically zero. For each dipole transition, the photoelectrons are thus completely spin polarized parallel to the surface normal.

The intensity for right-handed circular light reads

$$I(\sigma_+)=2(|M_6^{+-}|^2+|M_7^{-+}|^2), \tag{1}$$

where $M_i^{ss'}$ denotes the transition-matrix element from a $\Delta_i s'$ initial state with single-group symmetry Δ^5 into a $\Delta_6 s$ final state with single-group symmetry Δ^1. For left-handed circular light we obtain

$$I(\sigma_-)=2(|M_6^{-+}|^2+|M_7^{+-}|^2). \tag{2}$$

Equations (1) and (2) reflect the symmetry relation $I(\sigma_\pm,+\vec{M})=I(\sigma_\mp,-\vec{M})$, which is obvious from the mirror operations of the point group C_{4v}. Consequently, the intensity asymmetry, which constitutes MCDAD, can be obtained by reversing either the magnetization $\vec{M}$ or the light helicity. In the following we denote $I(\sigma_+,+\vec{M})$ and $I(\sigma_-,-\vec{M})$ as $I(\uparrow\uparrow)$, and $I(\sigma_+,-\vec{M})$ and $I(\sigma_-,+\vec{M})$ as $I(\uparrow\downarrow)$. According to Eqs. (1) and (2), $I(\uparrow\uparrow)$ consists of contributions from initial states of Δ_6^5- and Δ_7^5+ symmetry, and $I(\uparrow\downarrow)$ of those of Δ_6^5+ and Δ_7^5- symmetry. In the nonmagnetic limit, Kramer's degeneracy implies $M_i^{+-}=M_i^{-+}=:M_i$, with $i=6,7$, and the MCDAD vanishes, as it should.

C. Illustration of magnetic dichroism

More detailed insight into the physical origin of magnetic circular dichroism is provided in Fig. 1 by a typical set of numerical results for normal emission from perpendicularly magnetized Ni(001). In panel (a) the fully relativistic band structure is shown, calculated with the parameters mentioned above. The bands are distinguished according to their spin expectation value: thick (thin) solid lines indicate majority (minority) character, corresponding to a positive (negative) spin expectation value. The effect of the magnetization, i.e.,

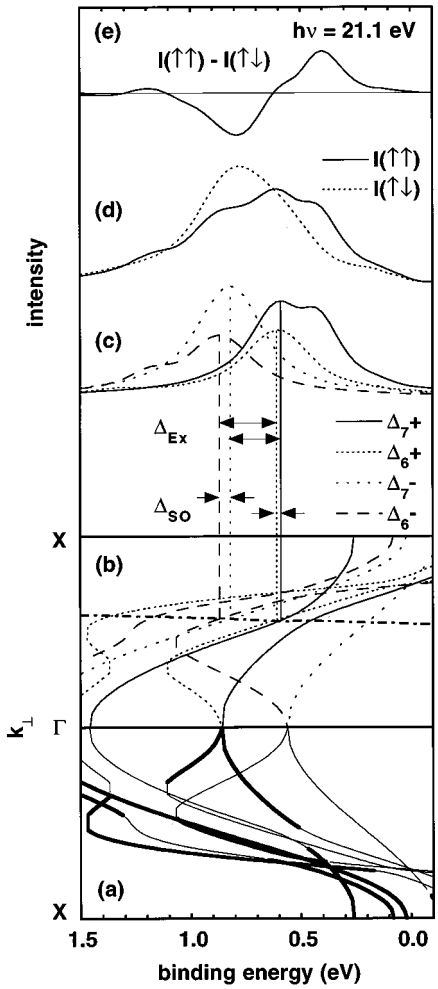

FIG. 1. Illustration of the origin of observed MCDAD. (a) Fully relativistic bulk band structure of Ni along the Δ axis with magnetization along the same axis, calculated with a real effective potential. Bands with majority- (minority-) spin expectation value are shown as thick (thin) solid lines. (b) As in (a), but with bands distinguished according to their double group symmetry as labeled in the figure. A final state band with mainly Δ^1 spatial symmetry, shifted downwards by 21.1 eV, is shown as dash-dotted line. The vertical lines mark crossing points of the final state band with four initial bands of predominating Δ^5 spatial symmetry (see text). The influence of spin-orbit (Δ_{SO}) and exchange interaction (Δ_{Ex}) is indicated by arrows. (c) Spin-resolved photoemission spectra for 21.1 eV photon energy, calculated with the above potential augmented by a uniform imaginary part describing the finite hole lifetime. Majority (minority) spin spectra are labeled as Δ_7- and Δ_6- (Δ_7+ and Δ_6+) in correspondence with the underlying initial-state bands, spectra for parallel (antiparallel) alignment of $\boldsymbol{\sigma}$ and $\mathbf{M}$ as Δ_7+ and Δ_6- (Δ_6+ and Δ_7-) bands (see text). (d) Calculated photoemission intensity spectra for parallel (solid line) and antiparallel alignment (dotted line) of photon spin $\boldsymbol{\sigma}$ and magnetization vector $\mathbf{M}$. (e) Difference of the two curves of (d).

the exchange splitting of 0.3 eV, is easily recognized. It is also obvious that the spin is no longer a ''good quantum number'' due to spin-orbit coupling, because some bands change from minority to majority character.

In panel (b) the same bands are distinguished according to their double-group symmetry Δ_7+, Δ_6+, Δ_7-, and Δ_6-. The final state band which is reached by photoexcitation is also shown as dash-dotted line, shifted downwards by 21.1 eV. In the direct transition model, which is useful for interpretation purposes, the initial state binding energy is given by the crossing points of this line with the initial state bands. As already mentioned, only bands with Δ^5 spatial symmetry contribute to the photoelectron spectra in the present totally symmetric geometry. Without spin-orbit and exchange coupling, there is only one band with this symmetry. This band is split by spin-orbit and exchange interaction into four energetically separated bands. The vertical lines in Fig. 1 originate at the crossing points of these four bands with the shifted final state band. Because of their prevailing spatial symmetry they can be labeled Δ_7^5+, Δ_6^5+, Δ_7^5-, and Δ_6^5-. The influence of spin-orbit (Δ_{SO}) and exchange interaction (Δ_{Ex}) is indicated by arrows between the vertical lines.

Figure 1 (c) shows calculated spin-resolved photoemission spectra for 21.1 eV photon energy. As discussed in the previous section, for parallel (antiparallel) alignment of photon spin and magnetization direction, only Δ_7^5+ and Δ_6^5- (Δ_6^5+ and Δ_7^5-) states contribute to the spectrum. The spin polarization of the respective photoelectrons is complete in the sense that Δ_7^5+ and Δ_6^5+ bands contribute to the minority-spin spectra, whereas Δ_7^5- and Δ_6^5- appear in the majority-spin spectra. The four resulting spectra are depicted in Fig. 1 (c), using the line types corresponding to the initial state double-group symmetry: Minority peaks are given by solid and dashed lines, corresponding to the nomenclature used for Δ_7+ and Δ_6+ symmetry, majority peaks by dotted and broken lines, corresponding to Δ_7- and Δ_6- symmetry. Sizeable peaks in the photoemission spectra in panel (c) are seen to be associated with the four discussed crossing points in panel (b). As can be seen, there are also significant contributions to the spectra at other than the marked crossing points. This is due to the fact that hybridization between bands of the same double-group symmetry but different spatial symmetry can occur, leading to a larger number of initial states containing Δ^5 spatial symmetry parts. At the photon energy of 21.1 eV, such hybridization is mainly observed in bands of Δ_7+ and Δ_6- double-group symmetry, leading to peaks at 0.45 and 1.2 eV binding energy, respectively.

Without spin resolution in the photoemission experiment, the spectra cannot be distinguished according to the electron-spin polarization as in Fig. 1 (c). As the calculated spin-integrated photoemission intensities in Fig. 1 (d) show, there is however a strong MCDAD, which still contains much information on the relativistic band structure. The solid (dotted) lines correspond to parallel (antiparallel) alignment of photon spin and magnetization direction [$I(\uparrow\uparrow)$ and $I(\uparrow\downarrow)$, respectively]. Each spectrum is the sum of the two corresponding spectra of panel (c): Δ_7+ and Δ_6- give $I(\uparrow\uparrow)$, Δ_6+ and Δ_7- give $I(\uparrow\downarrow)$.

The topmost panel of Fig. 1 represents MCDAD as the difference between the two curves of panel (d). It shows a pronounced minus feature at 0.8 eV binding energy, which is due to emission from Δ_7- and, to a lesser extent, from Δ_6+ states. The other large feature, a positive peak around 0.4 eV binding energy, is mainly due to emission from the higher Δ_7+ band, which crosses the shifted final-state band at this energy.

The above example clearly illustrates how spin-orbit and exchange interaction in conjunction with relativistic dipole selection rules lead to MCDAD. Comparison of the results of one-step photoemission calculations with the relativistic band structure shows that all of the observed spectral features can—via direct transitions—be correlated with the respective details of the electronic bulk band structure. Magnetic dichroism, which does not require the experimentally more cumbersome spin resolution of the photocurrent, hence is a powerful tool for analyzing the spin character of the initial states. While in the above example only bulklike states are relevant, we note that this also holds for photoemission from surface states and thin-film states, in which cases a similar interpretation, based on layer-resolved densities of states rather than the bulk band structure, can be given (see, e.g., Ref. 43).

IV. RESULTS

The left-hand side of Fig. 2 shows a series of experimental intensity spectra of 15 ML Ni on Cu(001) for different photon energies from 11.1 up to 27.4 eV. Spectra for parallel (antiparallel) alignment of the light helicity and the magnetization direction are represented by solid (dotted) lines, following the nomenclature already used in Fig. 1 (d). The vertical lines mark special peak positions which will be discussed later.

On the right-hand side, calculated photoemission spectra for the same photon energies are depicted. Again, spectra for parallel (antiparallel) alignment of the light helicity and the magnetization direction are depicted by solid (dotted) lines.

Good qualitative agreement between experimental and theoretical data can be stated already at first sight. The spectra for 11.1 eV photon energy display relatively sharp peaks just below the Fermi energy. With increasing photon energy a dispersion towards higher binding energies and a broadening of the peaks are observed. The higher intensity in the peak maximum of the dotted curves in the spectra from $h\nu=11.1$ up to 21.1 eV is reproduced well in the theory. From 19.1 to 27.4 eV photon energy, intensity for antiparallel alignment of photon spin and magnetization dominates the peak on the higher binding energy side in both the experimental and theoretical curves. Sharp structures are better resolved in the theoretical curves. A distinct MCDAD, that is the difference between dotted and continuous lines, is seen from both experimental and theoretical spectra. Although the MCDAD is significantly larger in theory, the qualitative agreement to the experimental one is quite good. The lower experimental MCDAD must be attributed to the limited energetic and angular resolution, to possible imperfections in film morphology, and to the background of inelastically scattered electrons not considered in the calculations. Further-

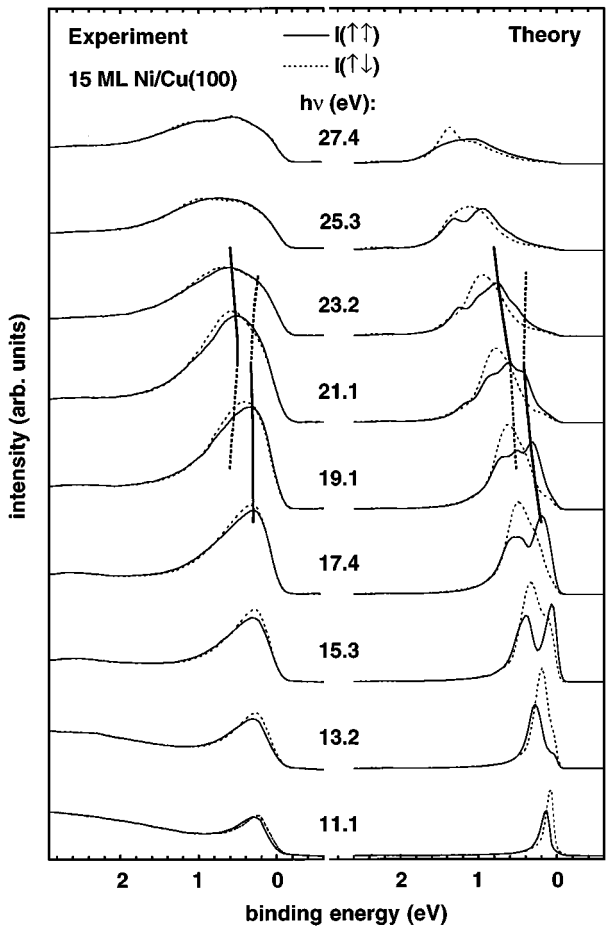

FIG. 2. Series of partial intensity spectra for different photon energies $h\nu$. Shown are spectra for parallel (solid lines) and antiparallel alignment (dotted lines) of photon spin and magnetization direction. Left: Experimental spectra, right: Theoretical spectra. The vertical lines indicate the occurrence of a hybridization region as explained in the text.

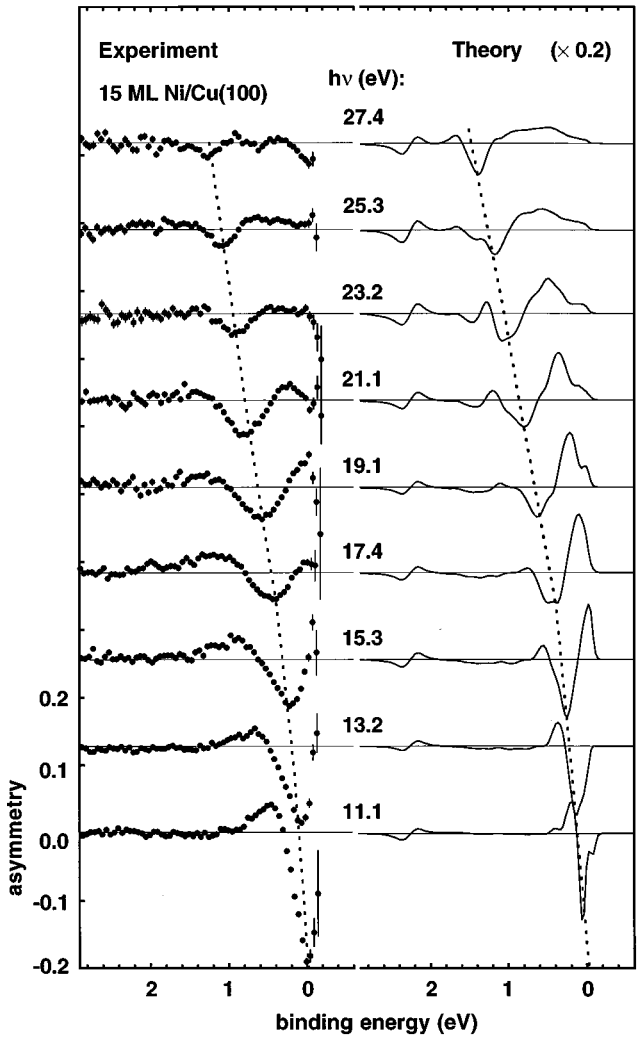

FIG. 3. Series of asymmetry spectra for different photon energies $h\nu$, calculated from the corresponding spectra of Fig. 2 as $[I(\uparrow\uparrow)-I(\uparrow\downarrow)]/[I(\uparrow\uparrow)+I(\uparrow\downarrow)]$. Left: Experimental asymmetries, right: Theoretical asymmetries (note the different scales). The vertical dotted lines mark the dispersion of the prominent minus peak.

more, the theoretical spectra were calculated for $T=0$ K and 100% circular polarization.

To visualize the dichroism more clearly, in Fig. 3 the normalized asymmetry of the spectra of Fig. 2 is shown. The normalized asymmetry A is defined as $A=[I(\uparrow\uparrow)-I(\uparrow\downarrow)]/[I(\uparrow\uparrow)+I(\uparrow\downarrow)]$. Again, experimental results are depicted on the left-hand side, theoretical on the right-hand side. We firstly note that the experimental spectrum at $h\nu=11.1$ eV shows an asymmetry of -20% near the Fermi edge, which is an unusually large dichroism for valence-band photoemission, and to our knowledge among the largest ever reported. To facilitate comparison with the experimental data, the theoretical asymmetry curves have been scaled down by a factor of 0.2. The original theoretical asymmetry values substantially exceed their experimental counterparts for the following reasons. Firstly, the experimental energy and angular resolution and the inelastic background, which have not been taken into account in our calculations, tend to reduce A. Secondly, the calculated A depends on the choice of the imaginary parts V_i of the optical potential for lower and upper states (with A decreasing for increasing V_i), and we have deliberately chosen a very small V_i for the lower states (below E_F) in order to make the connection of MCDAD with the band structure clearer (cf. Fig. 1). Apart from the thus-explained different scale, the agreement between experiment and theory in Fig. 3 is rather good. Several characteristics of the photon energy series can be seen in both the experimental and theoretical asymmetries. With increasing photon energy the asymmetry is reduced. We ascribe this mainly to the decrease of the lifetime of the initial states moving away from E_F and to a lesser extent to the decrease of the photoelectron lifetime with increasing kinetic energy. At all photon energies there is one pronounced minus feature, which disperses towards higher binding energies with increasing photon energy. The dotted vertical lines in Fig. 3 indicate the dispersion of this minus indentation. The experimentally observed dispersion is slightly smaller than the calculated one: At 11.1 eV photon energy the minus peak is located just below the Fermi edge in both experiment and theory, whereas at 27.4 eV it exhibits binding energies of 1.25 and 1.4 eV in experiment and theory, respectively. Its

absolute size shrinks with increasing photon energy. At 27.4 eV it amounts only to -2% in experiment and -20% in theory. For $h\nu \geq 15.3$ eV this minus peak is accompanied by plus peaks at both sides, the relative size of which differs between experiment and theory. They are seen most clearly at $h\nu = 19.1$ and 21.1 eV, and disperse together with the minus peak towards higher binding energies. From Fig. 3 it appears that the pronounced minus feature is too small (large) in the theoretical spectra (after reducing them by the factor 0.2) at low (high) photon energies. This discrepancy is, like the factor 0.2 itself, associated with the imaginary potential part V_i for the initial states, and indicates that the simple linear form, which we assumed in the absence of realistic first-principles knowledge, underestimates the increase of V_i with increasing binding energy.

In the theoretical spectra an additional plus/minus sequence around 2.3 eV binding energy is observed, which shows no dispersion. This asymmetry stems from emission from a surface resonance. It is not resolved in the experiment, which might be due to the relatively intense background of inelastic electrons compared to the low intensity of this resonance (cf. Fig. 2).

The dispersion of the asymmetry peaks and the observed plus/minus/plus feature can be understood from the illustrative picture of band symmetries and relativistic dipole selection rules mentioned in Sec. III C. In the case with no hybridization of the bands with Δ^5 spatial symmetry present, the situation is like the one shown in Fig. 1, but more symmetric. Only the four bands of Δ^5 spatial symmetry contribute in that case to the photoemission signal. When different lifetime broadening of states with different binding energies is ignored, the maximum of the minus peak in the dichroic asymmetry then gives the energetic position of the center of the bands with Δ^5 spatial symmetry, always disregarding possible hybridizations. The dispersion of this peak, indicated by dotted lines in Fig. 3, thus reflects the dispersion of the four bands with Δ^5 spatial symmetry. Its experimental observation allows an estimation of the band dispersion, which would be very difficult from intensity spectra alone (Fig. 2).

This example demonstrates that exploiting the magnetic dichroism already in the simple qualitative interpretation without access to relativistic photoemission calculations offers a significant plus of information with respect to conventional photoemission. Details of the band structure, however, or quantitative statements on the size of spin-orbit and exchange interaction can only be made with the help of relativistic calculations.

V. DISCUSSION

Before it is possible to deduce information about the spin-orbit and exchange split valence-band structure, the relation between the calculated photoemission spectra, obtained in a one-step formalism, and the fully relativistic band structure, calculated with the same parameters, has to be provided. As has been seen already from Fig. 1, the model of direct transitions serves to correlate specific details of the photoemission spectra to details of the relativistic band structure.

In Fig. 4 the theoretical band structure along the Δ axis from Fig. 1 is depicted on a larger scale. The bands are, like

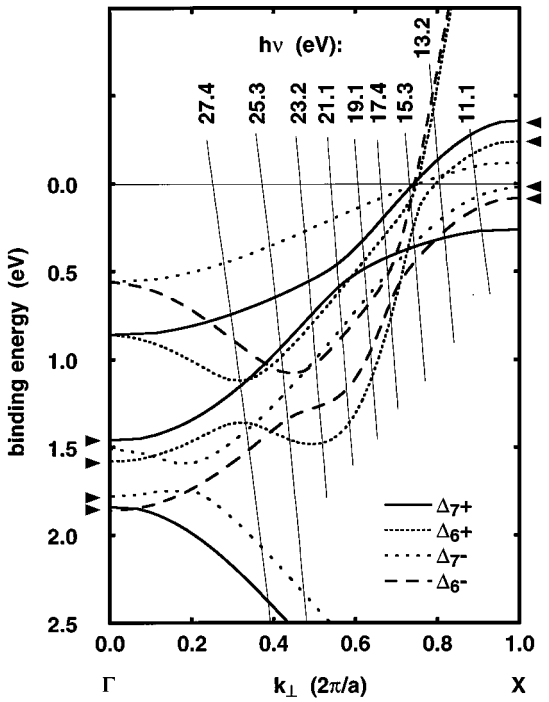

FIG. 4. Symmetry-resolved real valence band structure of Ni along the Δ axis, calculated with the same parameters as the photoemission spectra. Bands with Δ_7+, Δ_6+, Δ_7-, and Δ_6- double group symmetry are distinguished as labeled in the figure. The arrows indicate bands of Δ^5 orbital symmetry at X and Γ. The thin solid lines are sections of the final-state band, shifted down by the photon energy indicated at the respective line.

in Fig. 1 (b), again reproduced with differently dashed and dotted lines according to their double-group symmetry, as labeled in the figure. No classifications according to spin-occupancy or single-group symmetry are made. However, the four bands originating from the Δ^5 band in the nonrelativistic case, which lead to the dispersion of the minus peak in the asymmetry spectra, are marked by arrows on both sides of the panel: Starting at the Γ point, they have binding energies between 1.5 and 1.9 eV. When going along the Δ axis towards the X point, they disperse together upwards, interrupted by hybridization with other bands, to reach the X point at energies between 0.15 eV below and 0.3 eV above the Fermi energy. As the content of Δ^5 spatial symmetry of a band is necessary for the observation by photoemission in the present geometry, these bands and bands involved in hybridization with them are the origin of all of the observed spectra, as outlined before.

To facilitate the correlation with the photoemission spectra, nine sections of the calculated final-state band of Δ_6^1 symmetry, shifted down by the nine photon energies used in the experiment, are depicted in Fig. 4 by weak solid lines. As demonstrated in Fig. 1 for 21.1 eV photon energy, the crossings between these lines and the bands mark the energetic positions at which in the spectrum of the respective photon energy the transitions should be observed.

We will now first turn to the description of the band structure, which is essential in the qualitative interpretation of photoemission results. Because in Ni both exchange energy and spin-orbit coupling possess approximately the same

magnitude ($\approx$0.1–0.3 eV), the valence-band structure shows a lot of small band gaps, i.e., regions where bands of different single-group symmetry but identical double-group symmetry hybridize. Double-group theory implies that bands with the same double-group symmetry but different spatial symmetry couple due to spin-orbit interaction (e.g., Δ_7^2+, $\Delta_7^{2\prime}+$, and Δ_7^5+). Here, we will focus on electronic initial states with prominent Δ^5 spatial symmetry, because that is what we observe in the present experimental geometry.

In the energy range from -2 eV up to the Fermi level (0 eV), Δ_6+ initial states show spin-orbit induced band gaps at $k_\perp=0.30(2\pi/a)$ and at $k_\perp=0.75(2\pi/a)$, whereas Δ_6- initial states show such gaps at $k_\perp=0.45(2\pi/a)$ and $k_\perp=0.70(2\pi/a)$. For occupied bands with Δ_7+ (Δ_7-) symmetry there is only one gap around $k_\perp=0.55(2\pi/a)$ ($k_\perp=0.20\cdot 2\pi/a$).

Let us first consider the hybridization of bands with Δ_7+ symmetry. The hybridization gap is the result of an avoided crossing of bands with Δ^2 and Δ^5 spatial symmetry. The steeper Δ_7^5+ band of minority-spin character changes symmetry (and spin occupancy) with the flatter Δ_7^2+ majority band. This hybridization should occur in the photoemission spectra of 19.1 and 21.1 eV photon energy, as seen from Fig. 4. In Fig. 1 it was already demonstrated how both of the Δ_7+ bands in the hybridization region contribute to the photoelectron spectra. The vertical lines in Fig. 2 indicate the hybridization region. They mark the corresponding peaks in the photoemission intensity spectra for $\boldsymbol{\sigma}$ and $\mathbf{M}$ parallel [$I(\uparrow\uparrow)$, solid lines in Fig. 2]. The continuous lines show the positions of bands containing Δ_7^5+ symmetry, and fade out into dotted lines where the Δ_7^2+ symmetry character in these bands predominates. In the calculated spectra (right-hand side of Fig. 2), both of the hybridizing bands can be distinguished as separate peaks in the solid line spectra. It is clearly seen how the hybridization leads to an energetic displacement towards higher binding energies of the respective peak in the $I(\uparrow\uparrow)$ spectrum when the photon energy is increased from 17.4 to 23.2 eV. In the experimental spectra (left-hand side of Fig. 2), the hybridization occurs as energetic shift of the intensity weight of the peak in $I(\uparrow\uparrow)$ between 19.1 and 21.1 eV. Whereas at 19.1 eV the peak is asymmetrically shaped with higher weight at the low binding energy side, at 21.1 eV the weight is shifted to the side with higher binding energy. This leads also to an energetic shift of the first plus peak in the corresponding experimental asymmetry curves (left-hand side of Fig. 3) from 0.1 eV binding energy at $h\nu=19.1$ to 0.3 eV at $h\nu=21.1$ eV.

The next hybridization region we will discuss in more detail is the hybridization of Δ_6- bands. One of the hybridizing bands with Δ_6^- symmetry is the *sp*-like minority band with Δ^1 spatial symmetry which starts at the Γ point at $E_B\approx 0.6$ eV and reaches a minimum in binding energy at $k_\perp\approx 0.5(2\pi/a)$. It hybridizes with a band of Δ_6^5- symmetry, producing the two hybridization gaps at $k_\perp=0.45(2\pi/a)$ and $k_\perp=0.70(2\pi/a)$. Between these gaps both bands are separated by less than 0.35 eV. In this region, the bands have a low expectation value of the spin polarization, and exhibit a considerable mixing of spatial symmetry. Both bands contain thus a significant portion of Δ_6^5- symmetry, and should hence both appear in the photoemission spectra for parallel alignment of photon spin and magnetization direction, according to the double-group symmetry Δ_6-.

In the calculated photoemission spectra (right-hand side of Fig. 2), this hybridization can be followed in the $I(\uparrow\uparrow)$ spectra from 19.1 eV up to 25.3 eV photon energy. At lower photon energies, there is only one peak at the higher binding energy side of the solid curves. This peak is due to transitions from Δ_6- initial states. At $h\nu=19.1$ eV, and most clearly at $h\nu=21.1$ eV and $h\nu=23.2$ eV, this peak is split into two peaks, one of them producing a shoulder around 1.2 eV binding energy. This is the consequence of the hybridization, which leads to two bands of Δ_6- double-group symmetry having partially Δ^5 spatial symmetry. The shoulder at $E_B=1.2$ eV is due to emission from the lower of the two bands. The maximum separation of both bands should be observed at photon energies of 21.1 and 23.2 eV (cf. Fig. 4), which leads to the clear separation of the observed shoulders. At higher photon energies the hybridization is weaker, and the higher band consists of mainly Δ_6^1- symmetry. At $h\nu=25.3$ eV therefore only one peak as contribution from the Δ_6- bands is observed at 1.3 eV binding energy.

The hybridization induced shoulder is also seen in the experimental spectra of Fig. 2. It is most clearly identified at $h\nu=21.1$ eV at 1.2 eV binding energy, but shows up already at $h\nu=19.1$ eV. The separation of the different peaks is better in the calculated spectra, which may be a consequence of the experimental resolution. By comparison of experiment with theory, however, this shoulder in the experimental spectra is unequivocally identified as emission from the hybridizing Δ_6- bands.

The other hybridization regions of initial bands containing Δ^5 character which have not yet been discussed concern bands of Δ_7- and Δ_6+ double-group symmetry. The hybridization gap of the Δ_7- bands at $k_\perp=0.20(2\pi/a)$ should not be visible in the photon energy range used in the experiment (cf. Fig. 4). Transitions from Δ_6+ bands appear in the spectra for antiparallel alignment of photon spin and magnetization direction [$I(\uparrow\downarrow)$]. As the energetic sequence of the four Δ^5 containing bands is Δ_7^5+, Δ_6^5+, Δ_7^5-, Δ_6^5- (cf. Fig. 4), the emission from Δ_6^5+ and Δ_7^5- bands overlaps in the spectra to give one broad peak in the dotted curves of Fig. 2. It is therefore much more difficult to observe the hybridization of these bands. The hybridization of the Δ_6^5+ band with the *sp*-like Δ_6^1+ band which has a strong dispersion and an energetic minimum at $k_\perp\approx 0.5(2\pi/a)$ is in fact hardly observable in the photoemission spectra.

The comparison of experimental data with the calculated spectra enables us to draw specific information about the relativistic band structure from the experiment. Keeping in mind that certain experimental circumstances as, for example, the temperature and the experimental energetic as well as angular resolution are not considered in the calculations, the good qualitative agreement proves that the correlation of the experimentally observed features to the details of the band structure, as delineated in the previous section, is correct. Deviations between experiment and calculation can then be judged as experimental evidence for a distinct behavior of the system.

Such a deviation regards the dispersion of the observed dichroic structures (dotted lines in Fig. 3). The experimentally observed dispersion is about 0.15 eV smaller than the theoretical one. This can, however, either be explained by a different behavior of the lower or of the upper bands. Although the comparison of theory and experiment can also be used to judge the authenticity of the values taken for the real part of the inner potential, this is not accurate enough to decide between the two possibilities. The good agreement of the experimental and theoretical photon energies at which the Δ_7+ hybridization is observed (cf. Fig. 2), shows that the real part of the inner potential is basically well chosen. The small deviation of 0.15 eV in the dispersion of the initial bands may nevertheless still be assigned to both a slightly different behavior of the upper bands as well as a different dispersion of the valence bands.

The different dispersion in theory explains the disagreement in the height and the width of the first plus peak near the Fermi edge observed in the asymmetry spectra of Fig. 3. Especially at 15.3 and 17.4 eV photon energies this peak is much more pronounced in theory. This can be explained by the slightly stronger dispersion of the calculated photoemission peaks. In theory, the Δ_7^5+ band responsible for this plus structure is already significantly below the Fermi edge at these photon energies, whereas in the experiment full emission from that band is observed only at higher photon energies. Furthermore, the broader peaks due to experimental energetic resolution lead to a higher intensity of also the $I(\uparrow\downarrow)$ spectra at the Fermi edge and thus to a lower asymmetry.

Another property of the system which can be extracted from the present data concerns the hybridization between bands of the same double-group symmetry. The experimentally observed hybridization gaps agree very well with theory, so that the calculated band structure of Fig. 4 (or Fig. 1) is fully confirmed in this respect. The content of Δ^5 spatial symmetry in the hybridization regions, which is necessary for the experimental observation in the totally symmetric geometry, is also confirmed by the comparison of experiment with theory. It is for the sake of clarity not shown in the figures but principally also available.

Taking advantage of special points in the Brillouin zone, it is also possible to determine information about important parameters of the relativistic band structure. At 11.1 eV photon energy, for example, only two minority bands of Δ_7- and Δ_6- symmetry contribute to the spectra (cf. Fig. 4). They are energetically separated by the spin-orbit interaction, and appear each for a different alignment of photon spin and magnetization direction. The separation of the corresponding peaks in the experimental spectra for parallel and antiparallel alignment of $\boldsymbol{\sigma}$ and $\mathbf{M}$ (Fig. 2) is then an experimental measure of the strength of spin-orbit coupling in the valence bands. At that particular point of the Brillouin zone (50 ± 5) meV are obtained compared to 60 meV from the calculations. This is the same order of magnitude but nevertheless significantly smaller than the 100 meV obtained formerly for copper.[11,12]

It is more difficult to estimate an experimental value for the exchange splitting from the present spin-integrating measurements. The comparison with the calculations concerning the appearance of the bands below the Fermi edge and the positions of the hybridization gaps indicates that the value of 0.3 eV taken for the calculations is correct.

We have used Ni/Cu(001) as a prototype system to demonstrate the capability of valence-band MCDAD measurements supported by relativistic calculations. The perpendicular magnetization of this system allows us the direct correlation of the dichroism to the band structure. However, in systems with a lower symmetry, the content of information of MCDAD is similar. The comparison with relativistic calculations should also provide a detailed understanding of the electronic properties of the spin-orbit and exchange split system, even when a correlation with interband transitions is not possible.

VI. CONCLUSIONS

It has been shown, using Ni/Cu(001) as a prototype system, how from the comparison of experimental MCDAD data to fully relativistic calculations even fine details of the band structure can be resolved. Whereas the experiment alone is already capable to deliver qualitative information about the electronic structure, the access to fully relativistic calculations provides the possibility to extract specific information about the valence states. The dispersion of the Δ^5-type valence bands, the position and type of spin-orbit-induced hybridization gaps, and values for the strength of spin-orbit and exchange interaction and for the inner potential could be determined from the experiment that way. It was demonstrated how MCDAD in a totally symmetric arrangement is directly related to the relativistic band structure. The capability of magnetic circular dichroism in valence-band photoemission for the investigation of the exchange and spin-orbit split relativistic band structure of ferromagnets is thus proven.

ACKNOWLEDGMENTS

This work was supported by the German minister of education, science, research, and technology (BMBF) under Contracts No. 05 621EFA and No. 05 5PGABB7. We like to thank B. Zada for her technical assistance, and are indebted to the Freie Universität Berlin for its hospitality.

[1] C. S. Wang and J. Callaway, Phys. Rev. B **9**, 4897 (1974).

[2] B. Ackermann, R. Feder, and E. Tamura, J. Phys. F **14**, L178 (1984).

[3] L. Fritsche, J. Noffke, and H. Eckardt, J. Phys. F **17**, 943 (1987).

[4] P. Strange, H. Ebert, J. B. Staunton, and B. L. Gyorffy, J. Phys. Cond. Matter **1**, 2959 (1989).

[5] E. Tamura, W. Piepke, and R. Feder, Phys. Rev. Lett. **59**, 934 (1987).

[6] E. Tamura and R. Feder, Solid State Commun. **79**, 989 (1991); Europhys. Lett. **16**, 695 (1991).

[7] J. Henk and R. Feder, Europhys. Lett. **28**, 609 (1994).

[8] *Polarized Electrons in Surface Physics*, edited by R. Feder

(World Scientific, Singapore, 1985).
[9] N. Irmer, R. David, B. Schmiedeskamp, and U. Heinzmann, Phys. Rev. B **45**, 3849 (1992).
[10] D. Venus and H. L. Johnston, Phys. Rev. B **50**, 15 787 (1994).
[11] C. M. Schneider, J. J. de Miguel, P. Bressler, P. Schuster, R. Miranda, and J. Kirschner, J. Electron Spectrosc. Relat. Phenom. **51**, 263 (1990).
[12] W. Kuch, M.-T. Lin, K. Meinel, C. M. Schneider, J. Noffke, and J. Kirschner, Phys. Rev. B **51**, 12 627 (1995).
[13] L. Baumgarten, C. M. Schneider, H. Petersen, F. Schäfers, and J. Kirschner, Phys. Rev. Lett. **65**, 492 (1990).
[14] B. T. Thole and G. van der Laan, Phys. Rev. B **44**, 12 424 (1991).
[15] T. Scheunemann, S. V. Halilov, J. Henk, and R. Feder, Solid State Commun. **91**, 487 (1994).
[16] J. Henk, S. V. Halilov, T. Scheunemann, and R. Feder, Phys. Rev. B **50**, 8130 (1994).
[17] *Photoemission and the Electronic Properties of Surfaces*, edited by B. Feuerbacher, B. Fitton, and R. F. Willis (Wiley, New York, 1978).
[18] *Angle-Resolved Photoemission: Theory and Current Applications*, edited by S. V. Kevan (Elsevier, Amsterdam, 1992).
[19] G. van der Laan and B. T. Thole, Phys. Rev. B **48**, 210 (1993).
[20] N. A. Cherepkov, Phys. Rev. B **50**, 13 813 (1994).
[21] D. Venus, L. Baumgarten, C. M. Schneider, C. Boeglin, and J. Kirschner, J. Phys. Condens. Matter **5**, 1239 (1993).
[22] H. B. Rose, F. U. Hillebrecht, E. Kisker, R. Dennecke, and L. Ley, J. Magn. Magn. Mater. **148**, 62 (1995).
[23] M. Wöhlecke and G. Borstel, Phys. Rev. B **23**, 980 (1981).
[24] F. Meier, *Polarized Electrons in Surface Physics* (Ref. 8), p. 423.
[25] A. Eyers, F. Schäfers, G. Schönhense, U. Heinzmann, H. P. Oepen, K. Hünlich, J. Kirschner, and G. Borstel, Phys. Rev. Lett. **52**, 1559 (1984).
[26] C. M. Schneider, J. Garbe, K. Bethke, and J. Kirschner, Phys. Rev. B **39**, 1031 (1989).
[27] C. M. Schneider and J. Kirschner, Crit. Rev. Solid State Mater. Sci. **20**, 179 (1995).
[28] J. Henk, T. Scheunemann, S. V. Halilov, and R. Feder, J. Phys. Condens. Matter. **8**, 47 (1996).
[29] L. Néel, J. Phys. Rad. **15**, 376 (1954).
[30] U. Gradmann, J. Magn. Magn. Mater. **54–57**, 733 (1986); **100**, 481 (1991).
[31] P. Bruno and J. Renard, App. Phys. A **49**, 499 (1989).
[32] F. Huang, M. T. Kief, G. J. Mankey, and R. F. Willis, Phys. Rev. B **49**, 3962 (1994).
[33] W. L. O'Brien and B. P. Tonner, Phys. Rev. B **49**, 15 370 (1994).
[34] B. Schulz and K. Baberschke, Phys. Rev. B **50**, 13 467 (1994).
[35] B. Schulz, R. Schwarzwald, and K. Baberschke, Surf. Sci. **307–309**, 1102 (1994).
[36] G. Bochi, C. A. Ballentine, H. E. Inglefield, C. V. Thompson, R. C. O'Handley, H. J. Hug, B. Stiefel, A. Moser, and H.-J. Güntherodt, Phys. Rev. B **52**, 7311 (1995).
[37] J. Shen, J. Giergiel, and J. Kirschner, Phys. Rev. B **52**, 8454 (1995).
[38] F. Baudelet, M.-T. Lin, W. Kuch, K. Meinel, B. Choi, C. M. Schneider, and J. Kirschner, Phys. Rev. B **51**, 12 563 (1995).
[39] J. Shen, M.-T. Lin, J. Giergiel, C. Schmidthals, M. Zharnikov, C. M. Schneider, and J. Kirschner, J. Magn. Magn. Mater. (to be published).
[40] F. Schäfers, W. Peatman, A. Eyers, C. Heckenkamp, G. Schönhense, and U. Heinzmann, Rev. Sci. Instrum. **57**, 1032 (1986).
[41] S. V. Halilov, E. Tamura, H. Gollisch, D. Meinert, and R. Feder, J. Phys. Condens. Matter **5**, 3859 (1993).
[42] L. M. Falicov and J. Ruvalds, Phys. Rev. **172**, 498 (1968).
[43] J. Henk, T. Scheunemann, S. V. Halilov, and R. Feder, Phys. Status Solidi B **192**, 325 (1995); S. V. Halilov, J. Henk, T. Scheunemann, and R. Feder, Phys. Rev. B **52**, 14 235 (1995).